Journal of Geophysical Research: Solid Earth

RESEARCH ARTICLE

10.1029/2017JB015039

Key Points:

- Multistranded 1959 Hebgen Lake earthquake rupture reassessed with newly acquired airborne lidar topography data
- Morphologically simple scarp captures 1959 event and, in places, one or more Holocene paleo-earthquakes known from trenching
- The Hebgen-Red Canyon fault system ruptures with variable slip-per-event at a site

Supporting Information:

- Supporting Information S1
- Data Set S1
- Data Set S2
- Data Set S3

Correspondence to:
K. L. Johnson,
kendra430johnson@gmail.com

Citation:
Johnson, K. L., Nissen, E., & Lajoie, L. (2018). Surface rupture morphology and vertical slip distribution of the 1959 M_w 7.2 Hebgen Lake (Montana) earthquake from airborne lidar topography. *Journal of Geophysical Research: Solid Earth*, *123*, 8229–8248. https://doi.org/10.1029/2017JB015039

Received 27 SEP 2017
Accepted 2 AUG 2018
Accepted article online 9 AUG 2018
Published online 22 SEP 2018

Surface Rupture Morphology and Vertical Slip Distribution of the 1959 M_w 7.2 Hebgen Lake (Montana) Earthquake From Airborne Lidar Topography

Kendra L. Johnson[1,2], Edwin Nissen[3], and Lia Lajoie[2]

[1]Now at GEM Foundation, Pavia, Italy, [2]Department of Geophysics, Colorado School of Mines, Golden, CO, USA, [3]School of Earth and Ocean Sciences, University of Victoria, Victoria, Canada

Abstract The 1959 M_w ~7.2 Hebgen Lake earthquake is among the largest continental normal faulting events recorded, as well as one of the earliest associated with a multifault rupture. Multimeter vertical slip was observed on three main, morphologically distinct strands: the Hebgen fault and southeastern section of the Red Canyon fault, which both follow sharp topographic rangefronts, and the Red Canyon fault Kirkwood Ridge section, which cuts steep topography in the footwall of the Hebgen fault. We augment early field, seismological, and geodetic studies by investigating the modern surface rupture using newly acquired airborne lidar topography. By estimating throw from scarp profiling of the ~36.5 km primary surface rupture, we show both that peak 1959 slip occurred at a structurally mature part of the fault and that many 1959 slip minima are associated with clear structural complexities. Vertical slip often substantially exceeds throw measured at the fault free face immediately after the earthquake; the scarps do not conclusively express beveled forms characteristic of repeated slip and degredation, yet must in places capture both the 1959 earthquake (for which we estimate an average throw of 2.64 m) and one or two preceding latest Pleistocene–Holocene events known from trenching. This has wider, cautionary implications for interpreting paleo-earthquake chronologies and deriving magnitudes from morphologically simple scarps. By comparing 1959-only and multievent vertical displacement populations, and considering preliminary paleoseismic data, we suggest that large surface-rupturing earthquakes on the Hebgen and Red Canyon faults involve highly variable slip distributions.

1. Introduction

Surface ruptures are normally the only place where we can directly observe earthquake faulting. Critical aspects of the earthquake process may be expressed in its surface rupture, including source complexity (e.g., Fletcher et al., 2014; Hamling et al., 2017), rupture propagation dynamics (e.g., Elliott et al., 2009; Wesnousky, 2006), material strains (e.g., Oskin et al., 2012; Shaw, 2011), fault damage zone development (e.g., Dolan & Haravitch, 2014; Vallage et al., 2015), and slip histories over multiple earthquake cycles (e.g., Benedetti et al., 2013; Klinger et al., 2011; Manighetti et al., 2015; Salisbury et al., 2012).

Modern optical satellite imagery enables surface faulting sampling at much higher spatial densities (~100s of measurements over ~10s of kilometers) than is typically possible with field mapping. *Before* and *after* photograph subpixel correlation, now routine for modern large earthquakes, can provide a high-resolution horizontal deformation field from which surface slip can be sampled (Leprince et al., 2008). However, these methods retrieve only horizontal displacements, and so have been applied predominantly to strike-slip earthquakes. Recovering vertical slip along dip-slip earthquakes is more challenging, because it relies upon three-dimensional (3-D) surface topography or stereo imagery rather than merely two-dimensional surface texture. This dependence on less available 3-D data has restricted high-density, geodesy-based surface slip profiling of dip-slip earthquakes to just a few events (Chen et al., 2001; Haddon et al., 2016; Hollingsworth et al., 2012; Kaneda et al., 2008; Nissen et al., 2014).

Here we reassess the 1959 M_w 7.2 Hebgen Lake earthquake surface rupture using new submeter resolution airborne lidar topography. This event remains one of the largest continental normal faulting earthquakes recorded globally, and possibly the largest of any type to occur in the United States outside of Alaska or California during the instrumental period (since ~1900). It is also one of the first earthquakes known to have involved slip on multiple, separate faults, with three main strands and a few shorter ones, and so this earthquake could complement more recent observations of cascading rupture behavior (e.g., Fletcher et al., 2014; Hamling et al., 2017; Nissen et al., 2016). However, though it was among the first earthquake ruptures surveyed in great detail in the field (Myers & Hamilton, 1964; Witkind et al., 1962; Witkind, 1964), a dense slip distribution has never been compiled.

We map the surface rupture as it is preserved >50 years after the earthquake and present hundreds of new measurements of the vertical slip. We find that the scarp in places preserves evidence for pre-1959 Holocene earthquakes, and consequently we interpret our surface throw distribution not only in terms of the 1959 earthquake, but also in the context of preliminary paleoseismic trench results (Haller et al., 2002; Hecker et al., 2002; Pierce et al., 2000; Schwartz et al., 2009). This enables us to investigate whether previous ground-rupturing earthquakes along the 1959 faults had similar slip distributions and rupture lengths.

2. Earthquake Background

The M_w 7.2 Hebgen Lake earthquake occurred at 11:37 P.M. local time on 17 August 1959 in southern Montana (Figure 1a). Though far from any large town, this popular summer vacation spot was busy with campers at the time of the earthquake. The earthquake triggered a major landslide, the Madison Slide, that buried several campers and dammed the Madison River, rapidly forming Earthquake Lake or *Quake Lake* (Figure 1b). Flooding was exacerbated by a seiche that overtopped the dam of the Hebgen Lake reservoir upstream. In total, at least 28 people were killed or missing.

2.1. Regional Tectonics and Geology

Hebgen Lake is situated within the Centennial Tectonic Belt (Figure 1a), an area of diffuse, mostly NW-SE-trending normal faulting separated from the larger Basin and Range extensional province by the aseismic Snake River Plain (Stickney & Bartholomew, 1987). GPS velocities show NE-SW-oriented extension of ~3 mm/year over the whole Centennial Tectonic Belt (e.g., Payne et al., 2012; Schmeelk et al., 2017). Derived block models assign the most important individual fault slip rates of ~1 mm/year, but GPS velocities around Hebgen Lake are still dominated by postseismic deformation from the 1959 earthquake, preventing firm constraints on strain accumulation rates in this vicinity (Schmeelk et al., 2017).

The Hebgen Lake region contains an ~2,000 m thick Paleozoic and Mesozoic sedimentary sequence underlain by metamorphic basement (Witkind et al., 1964). During the late Cretaceous Laramide orogeny, the Madison Range was thrust eastward along the Cabin Creek zone, a narrow (~5 km wide) belt of folding and faulting that traverses the parallel Hebgen and Kirkwood ridges NE of Hebgen Lake (Figure 1b). Hebgen ridge is flanked to the northeast by the Wells fault, and to the southwest by the Johnson fault, both SW-dipping Laramide thrusts. Neither is well exposed, but Witkind et al. (1964) tentatively ascribe the Wells fault a dip of 20°–50°. Hebgen ridge itself is composed mostly of subvertical, vertical, or overturned Mississippian to Permian strata. The arcuate Kirkwood ridge is likewise bound to the northeast by a Laramide thrust, the ~20° SW-dipping Divide fault. Mississippian to Triassic strata outcrop near the ridge crest, folded and overturned such that they dip south or southwestward. Extension associated with the modern Centennial Tectonic Belt started in the Miocene and has led to formation of graben and half-graben along steep normal faults. Early studies of the Hebgen Lake earthquake took interest in the extent to which older Laramide structures guide the modern faulting (e.g., Myers & Hamilton, 1964; Witkind, 1964).

2.2. 1959 Surface Ruptures

The Hebgen Lake earthquake surface rupture was among the first to be mapped in detail immediately after the event. The following description, unless indicated otherwise, reflects the early reconnaissance by Witkind et al. (1962) and subsequent companion papers by Witkind (1964) and Myers and Hamilton (1964). The earthquake produced two main surface breaks: an ~10-km Hebgen fault rupture and an ~23-km Red Canyon fault rupture; these faults partially overlap, such that the end-to-end straight line rupture length is ~24 km (Figure 1b). The Hebgen fault is a SW-dipping normal fault that form the sharps, southern rangefront of Hebgen ridge and Mount Hebgen, with Hebgen Lake in its hangingwall. Its surface trace thus closely parallels the Laramide Johnson thrust. The Red Canyon fault is a subparallel SW-dipping normal fault separated into two arcuate segments: a ridge section high up the southern flank of Kirkwood ridge and a southeastern section bordering the Grayling Arm of Hebgen Lake. Hart et al. (2012) speculated that the Red Canyon scarp instead marks the headwall of a major landslide reactivated in the earthquake, but we find no support for this interpretation for reasons discussed later. Shorter ruptures (<1 and ~3 km) occurred on the structurally and

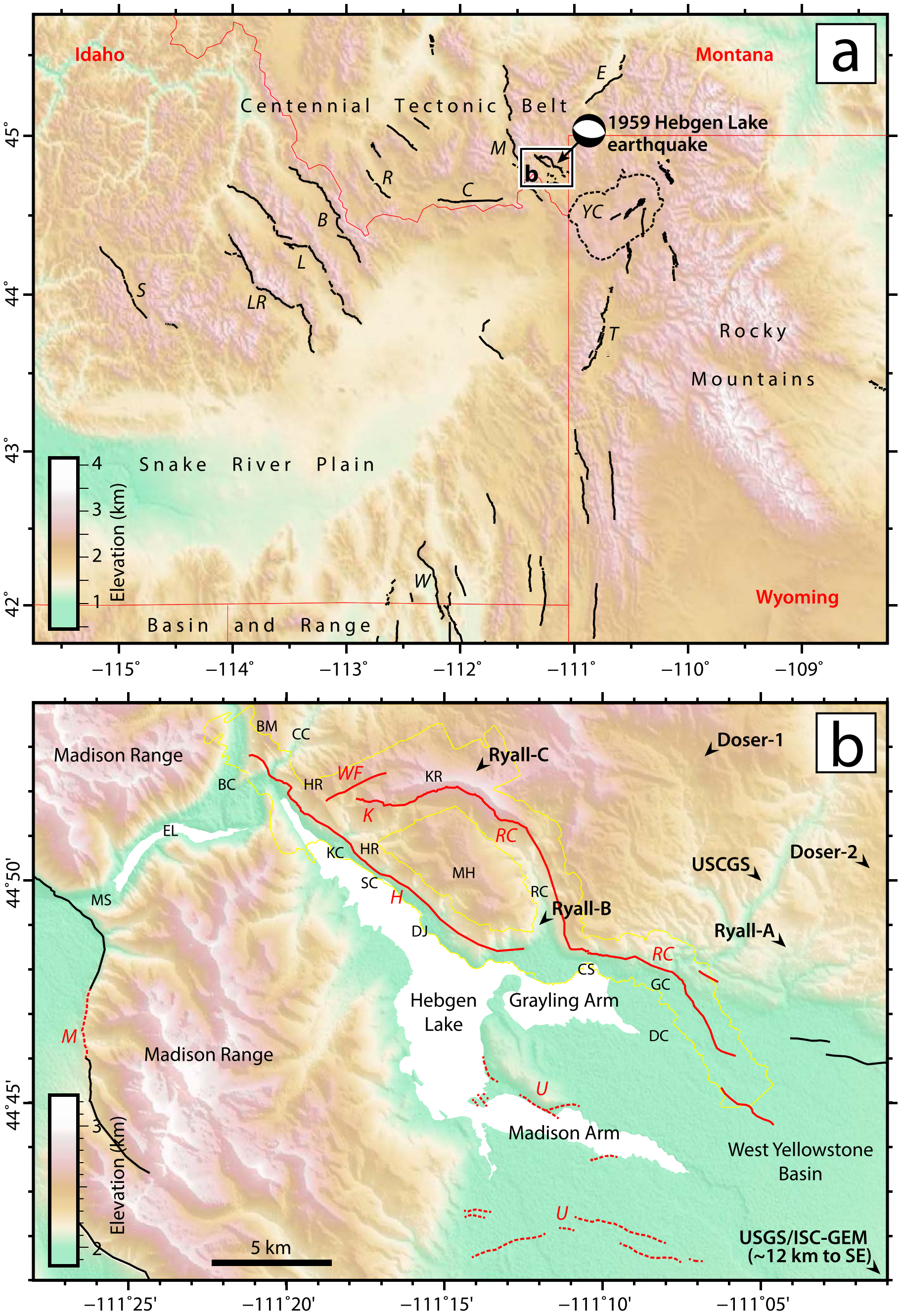

Figure 1. (a) Regional topography with late Quaternary faults from Haller et al. (2004) and a first motions mechanism for the 1959 Hebgen Lake earthquake from Ryall (1962). Major normal faults of the Centennial Tectonic Belt, with labels in the hangingwall, are: B, C, E, L, LR, R, and S. Elsewhere, YC, T, and W. (b) Overview of the 1959 earthquake epicentral region, including epicenter estimates (arrows) from Doser (1985) and Ryall (1962), the USCGS, and the contemporary USGS and ISC-GEM catalogs; primary surface rupture trace (red) on the Hebgen (H), Red Canyon (RC), Kirkwood (K), and West Fork (WF) faults; minor slip (red dashes) on the Madison fault (M) and unnamed faults south of Hebgen Lake (U); and lidar coverage (yellow). Other geographical features are as follows: BC = Beaver Creek; BM = Boat Mountain; CC = Cabin Creek; CS = Corey Spring; DC = Duck Creek; DJ = Dave Johnson Creek; EL = Earthquake Lake; GC = Grayling Creek; HR = Hebgen Ridge; KC = Kirkwood Creek; KR = Kirkwood Ridge; MH = Mount Hebgen; MS = Madison Slide; RC = Red Canyon Creek; SC = Section 31 Creek. B = Beaverhead; C = Centennial; E = Emigrant; L = Lemhi; LR = Lost River; R = Red Rock; S = Sawtooth; YC = Yellowstone Caldera; T = Teton fault; W = Wasatch fault; USCGS = United States Coast and Geodetic Survey; USGS = United States Geological Survey; ISC-GEM = International Seismological Centre-Global Earthquake Model.

topographically indistinct Kirkwood and the West Fork faults, SE-dipping structures near the western end of the Red Canyon fault. The earthquake also triggered minor (<1 m) slip along a short stretch of the Madison fault and on unnamed, scattered faults south and southeast of Hebgen Lake (Witkind et al., 1962), but this far-field deformation lies outside the scope of this paper.

Scarps mostly cut colluvial or alluvial deposits downslope from the bedrock contact, forming 50°- to 90°-dipping free faces that were documented shortly after the earthquake (Myers & Hamilton, 1964; Witkind et al., 1962; Witkind, 1964). Discontinuous open fissures, faulted graben, and slumped depressions were observed along the foot of the scarp, reflecting a tendency of the fault to steepen (*refract*) toward the free surface, causing the hangingwall to pull away from the footwall. Witkind (1964) measured the scarp height at ~60 roughly evenly spaced locations, using *relatively crude geological methods* (no further details are given). Each measurement is presented both with and without an adjustment for the slumping effect; peak scarp heights of 6.1 m on the Hebgen fault and 5.8 m on the Red Canyon fault are thus modified to vertical surface displacements of 5.8 and 4.6 m, respectively. Myers and Hamilton (1964) estimated the steepening in fault dip angle to be ~10° based on the magnitude of the slumping effect, and Witkind (1964) observed that the fissures are typically ~1.6–2 times deeper than they are wide, which would imply an underlying fault dip of ~60° (compared to the average surface dip of ~70°). However, slickensides were also observed on the scarp free face in some places (Witkind, 1964), and in such locations, any opening was presumably negligible. These lineations consistently indicate vertical (dip slip) motion with little or no horizontal component.

Witkind et al. (1962), Witkind (1964), and Myers and Hamilton (1964) also observed extensive off-fault deformation including secondary scarps and fissures, especially within the hangingwall of the principal rupture. Fissure density appears influenced by the underlying geology, with simple scarps atop steeply dipping underlying strata (favorably oriented for slip) and wider fissure zones where strata dip gently. In a few places, there is no principal scarp, and the rupture splays into several strands with only a few centimeters of slip on each. Where the rupture is closest to the bedrock-colluvium contact, prisms of colluvium remained attached to the bedrock in the footwall of the scarp at least through the initial reconnaissance. Occasionally, thick surficial deposits deflect the scarp uphill of projected bedrock faults, using the underlying bedrock-colluvium contact as a sliding plane. Parts of the rupture abut this contact and exploit pre-existing joint surfaces or bedding planes, such as along the ridge section of the Red Canyon fault, where displacement occurs along overturned Paleozoic strata.

In a few places, the 1959 rupture was visibly colocated with older, degraded fault scarps (Myers & Hamilton, 1964; Witkind, 1964). Near its southeastern termination within glacial outwash deposits of the West Yellowstone Basin, the Red Canyon rupture is superimposed upon a degraded scarp of similar height, which likely formed in the previous event (or events). This composite double-event scarp itself lies at the base of a much larger (~20 m) embankment—presumably representing several preceding earthquakes—that was cut backward by an old course of Grayling Creek. Degraded pre-1959 scarps were also evident west of Corey Spring on the Red Canyon fault, and at the toe of the Kirkwood Creek fan on the Hebgen fault, but the main 1959 rupture is not superimposed on these.

2.3. Seismology

The mainshock was initially assigned a magnitude of M_L 7.1 by the United States Coast and Geodetic Survey based on regional recordings (Fraser, 1964). This was upgraded to M_s 7.5 and M_w 7.3 based on waveform modeling and geodetic data (Barrientos et al., 1987; Doser, 1985), and the earthquake is currently listed as M_w 7.2 in the contemporary United States Geological Survey (USGS) and International Seismological Centre-Global Earthquake Model (ISC-GEM) catalogs (Storchak et al., 2015). The initial United States Coast and Geodetic Survey epicenter lies ~5 km north of the eastern Red Canyon rupture terminus (Murphy & Brazee, 1964; Figure 1b). Ryall (1962) relocated the epicenter, producing two revised estimates that lie within ~1 km of the Red Canyon rupture trace, and noted that the earthquake likely comprised two distinct subevents separated by ~5 s. Reexamining regional and teleseismic data, Doser (1985) assigned the first subevent m_b 6.3 and the second m_b 7.0. Though her own absolute epicenters are misplaced, lying northeast of the SW-dipping surface faults, she did obtain precise *relative* locations and found that the second subevent initiated 5–8 km south of the first. The current (single event) epicenters listed by the USGS and ISC-GEM are badly mislocated, ~15 km southeast of the surface rupture (Figure 1b). The widespread of epicenters prevents a confident assessment of lateral rupture directivity, although the location of many to the east or southeast of the surface rupture hints at an overall northwestward directivity (Doser, 1985).

Using *P*-wave first motions, Ryall (1962) resolved a SW-dipping nodal plane with strike 100° ± 10° and dip 54° ± 8° (Figure 1a). The hypocenter depth is poorly constrained by the sparse near-source data, but Ryall (1962) was able to define a maximum value of ~25 km. Doser (1985) used short-period first motions to resolve fault geometry at the hypocenter and long-period teleseismic body waveforms to constrain a centroid mechanism and depth for both subevents. She concluded that both initiated on fault planes with strike 102° ± 5° and dip 60° ± 5° SW. The first subevent then propagated onto a fault with strike 95° ± 5° and dip 42° ± 5°, and the second onto a fault with strike 93° ± 5° and dip 48° ± 5°. Neither Ryall (1962) nor Doser (1985) state numerical values for rake; most of their graphical solutions seem to imply pure normal slip, although Doser's waveform modeling solutions show a small component of left-lateral slip. She obtained centroid depths for the two subevents of 10 ± 2 km and 15 ± 3 km; the lower bounds of these ranges seem most plausible given that the ~15 km local seismogenic layer thickness as defined by maximum focal depths recorded by a subsequent microseismic deployment (Trimble & Smith, 1975). Doser (1985) suggests that the Red Canyon and Hebgen faults merge at depth into a single fault on which both subevents nucleated, but admits that the subsurface fault geometry and rupture history of the two subevents cannot be confidently recovered from the relative hypocentral locations, centroid depths, and focal mechanisms, given their uncertainties.

2.4. Geodesy

Myers and Hamilton (1964) contoured the vertical surface deformation field from measurements of the relative pre-earthquake Hebgen Lake shoreline submergence and benchmark releveling. They recorded maximum subsidence of ~6.7 m on the northern shoreline adjacent to the central Hebgen fault, and lesser values of ~4.0 and ~1.5 m in the Grayling and Madison Arms. Where the surface faults parallel the lake shoreline, hangingwall subsidence exceeds adjacent scarp heights except for the very peak values. Adding to the shoreline measurements with far-field leveling line data, Barrientos et al. (1987) inverted the surface deformation field for subsurface fault geometry. Their preferred elastic dislocation model comprises two rectangular, uniform-slip planes: 8 m of normal slip on an 18 km long Red Canyon fault plane striking 136° and dipping 45° from 1.7 to 10 km depth, and 7 m of normal slip on the 18 km long Hebgen fault plane striking 128° and dipping 50° SW from 0.3 to 12 km depth. The geodetic data permit, but do not require, a listric subsurface geometry for the Red Canyon fault, and support a planar Hebgen fault, such that it is possible, but not required, that the two merge at depths of a few kilometers—much like in the seismological modeling of (Doser, 1985). The ~30°–40° discordance in strike between the nodal planes from seismology (Doser, 1985) and the dislocations from geodesy (Barrientos et al., 1987) presumably reflects some additional subsurface complexity unaccounted for by either simplified models.

2.5. Scarp Degradation and Paleoseismic Record

Resurveying parts of the scarp ~20 and ~50 years after the earthquake, Kogan and Bendick (2011) and Wallace (1980) noticed that stable debris slopes of ~40° now characterized the central part of the scarp, helping fill in and cover over the original fissures and depressions. Wallace (1980) observed a small free face in a few localities, still intact high on the scarp, but retreated upslope from its original position. Nash (1984) surveyed some of the unnamed fault scarps south of Hebgen Lake that were reactivated in 1959 and estimated a penultimate event age of ~2.8 ka on one from morphologic dating.

Using cosmogenic ^{36}Cl exposure ages from a limestone scarp on the Hebgen fault southeast of Section 31 Creek, Zreda and Noller (1998) argued for five Holocene earthquakes (with ages ~7.0, ~2.6, ~1.7, and ~0.4 ka, and 1959) and two latest Pleistocene events (~24 and ~20 ka), each with 1–2 m of slip. However, three conventional paleoseismic trench studies contest the Zreda and Noller (1998) results, finding evidence for just three earthquakes since the latest Pleistocene (including 1959) at Section 31 Creek on the Hebgen fault and Grayling Creek on the Red Canyon fault (Haller et al., 2002; Hecker et al., 2002; Schwartz et al., 2009), and just two (including 1959) at Cabin Creek (Pierce et al., 2000). The pair of earlier events are radiocarbon dated at 1–3 ka and 10–15 ka. The excavated surfaces at Section 31 Creek and Grayling Creek are late Pleistocene based upon exposure dating, while the one at Cabin Creek is considered early Holocene or older based upon soil characteristics; it is therefore uncertain whether or not the 10–15 ka earthquake ruptured at Cabin Creek. Though these records are preserved below ground, scarps associated with the penultimate earthquakes—visible in photographs taken soon after the 1959 earthquake—are now largely removed by upslope retreat of the free face, leaving a morphologically simplified scarp that in places represents at least two earthquakes (Hecker et al., 2002; Schwartz et al., 2009). We return to this important point in our analysis and discussion of the lidar topography.

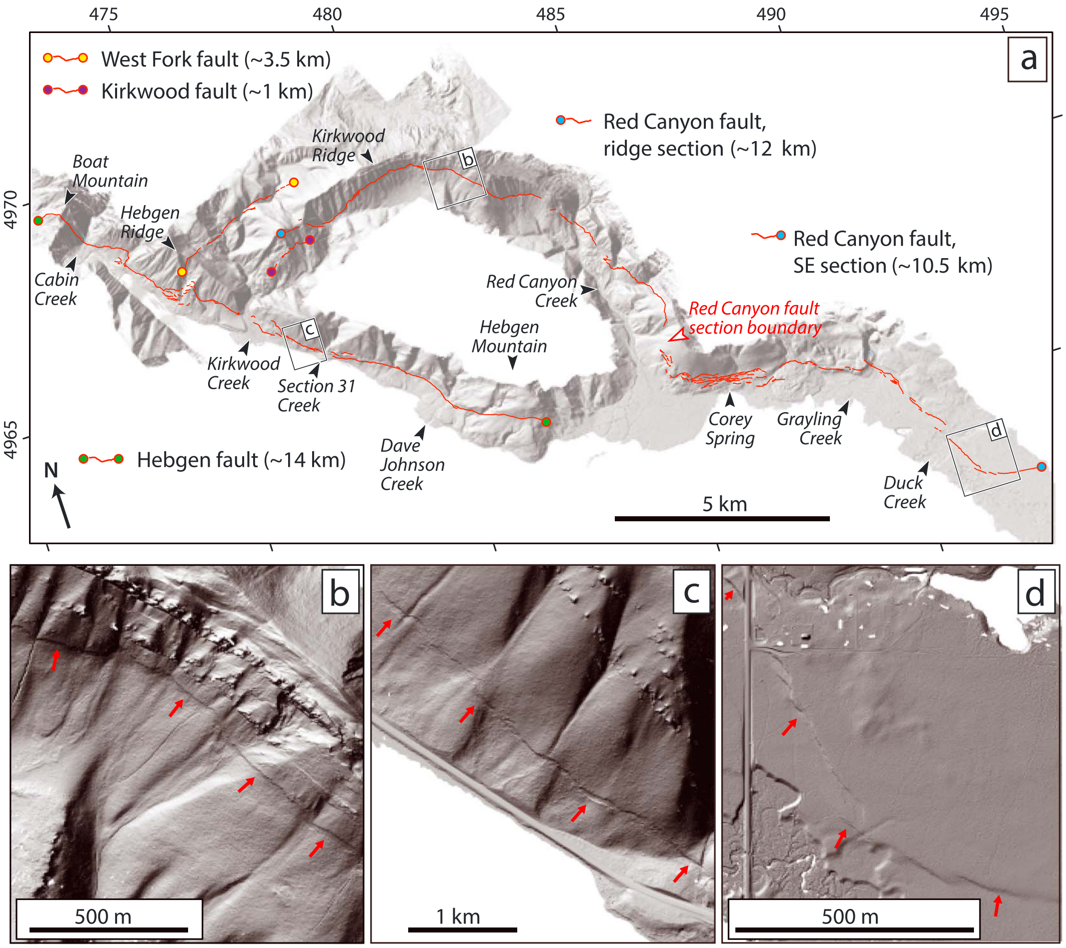

Figure 2. (a) Airborne lidar bare-earth Digital Elevation Model with 0.5 m spatial resolution, artificially illuminated from the north, with 1959 surface rupture traces in red. Horizontal coordinates for this map and all subsequent ones are Universal Transverse Mercator Zone 12 Eastings and Northings in kilometers. (b), (c), and (d) show details of surface rupture at three example localities, with red arrows pointing to the scarp.

3. Data and Methods

3.1. Airborne Lidar Survey and Rupture Mapping

Airborne lidar topographic data were collected over most of the 1959 surface rupture in October 2014 by the National Center for Airborne Laser Mapping (Figures 1b and 2a). Laser returns were collected with an Optech Titan multispectral sensor flown at 750–1200 m above ground level, yielding a swath width of 850–1,400 m with at least 50% overlap between adjacent swaths. Delivered data include a 7–11 points per square meter classified point cloud and a 0.5 m resolution bare-earth Digital Elevation Model, both available through the OpenTopography portal. The ~62.5 km^2 survey covers the full extent of the Hebgen, Red Canyon, Kirkwood, and West Fork ruptures, but does not capture minor slip on unnamed faults around the Hebgen Lake Madison Arm, or on the Madison fault to the southwest.

We begin our lidar data analysis by manually mapping the 1959 rupture on artificially illuminated Digital Elevation Models, capturing a discrete surface rupture along some traces and wider rupture zone with slumping, antithetic faulting, and splaying on others. We do not extrapolate or project the fault trace across gaps in the visible surface scarp.

3.2. Vertical Slip Distribution

We begin by extracting scarp-perpendicular topographic profiles from the airborne lidar DTM at 30-m intervals along our mapped rupture, avoiding obvious irregularities such as jogs or step overs. We project 3 m wide topographic swaths from the gridded lidar onto each profile and henceforth using the mean swath elevation, aiming to eliminate high-frequency topographic scatter produced by small-scale surface texture and

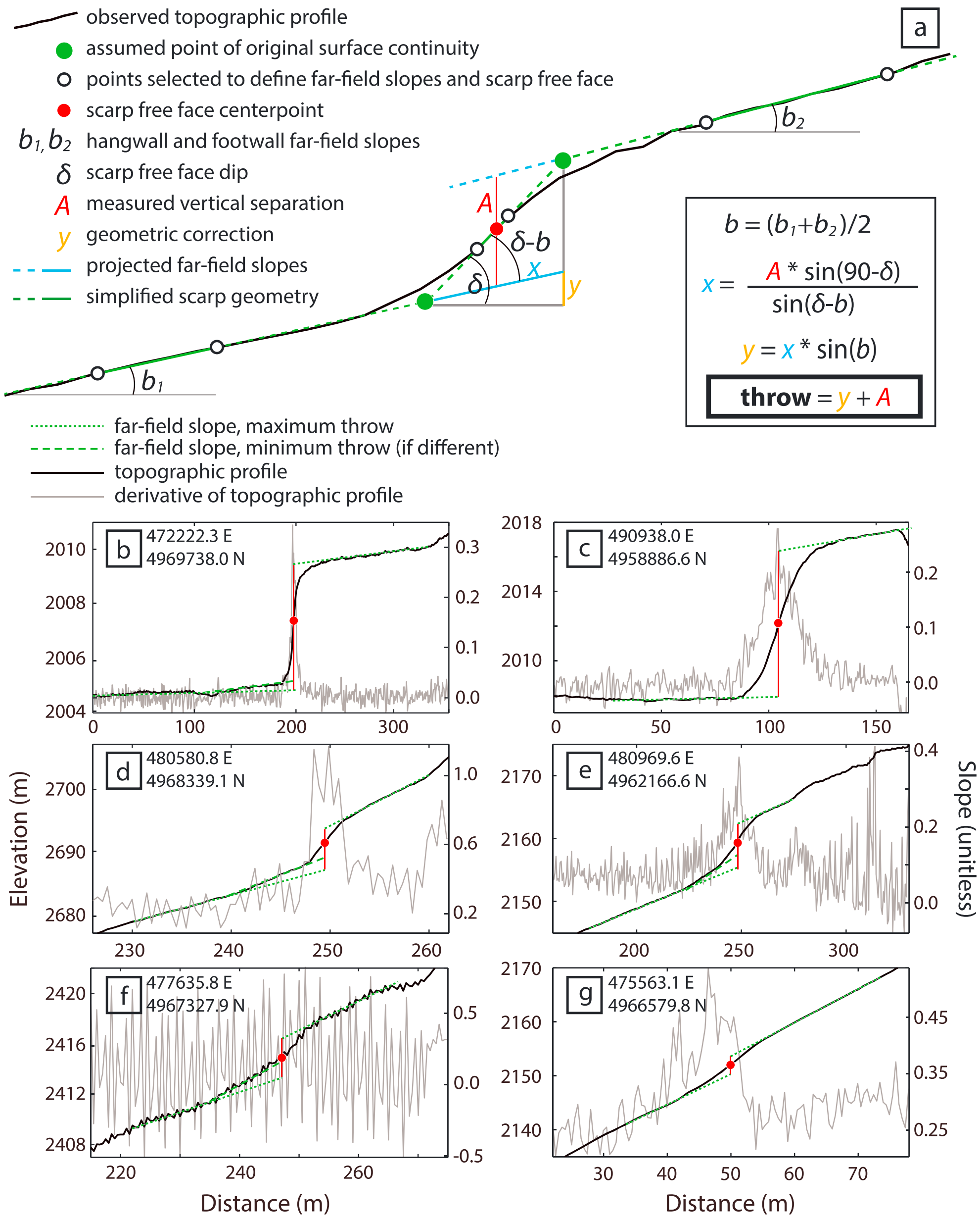

Figure 3. (a) Schematic of routine used to define scarp geometry and derive throw, modified from, for example, Baljinnyam et al. (1993) and Thompson et al. (2002). The black line is the observed scarp profile in its current, degraded state. Open circles are user-picked points that define the far-field slopes, and the scarp face. Solid green lines are straight lines fit through the profile between each pairs of user-picked points. Dashed green lines project the lines to their intersections, where solid green circles mark the points at which the pre-1959, unfaulted surface was originally continuous. The solid red circle is the lateral center point between the two green circles, and marks the scarp center point. Vertical separation *A* is measured as the vertical distance between the projected hanging and footwall slopes at the scarp center point. δ is fault dip, normally chosen as 60°; *b* is the averaged far-field slope; and *y* is the geometric correction—derived from the law of sines—added to *A* to recover fault throw. (b)–(g) Example profiles centered on the UTM Zone 12 coordinates listed in upper left of each frame. Profile locations are shown along the throw distribution in Figure 8. Black lines show the topographic profiles, annotated with far-field slopes (green) and vertical separation *A* (red). Gray lines show the slope (i.e., the first derivative of the profile topography).

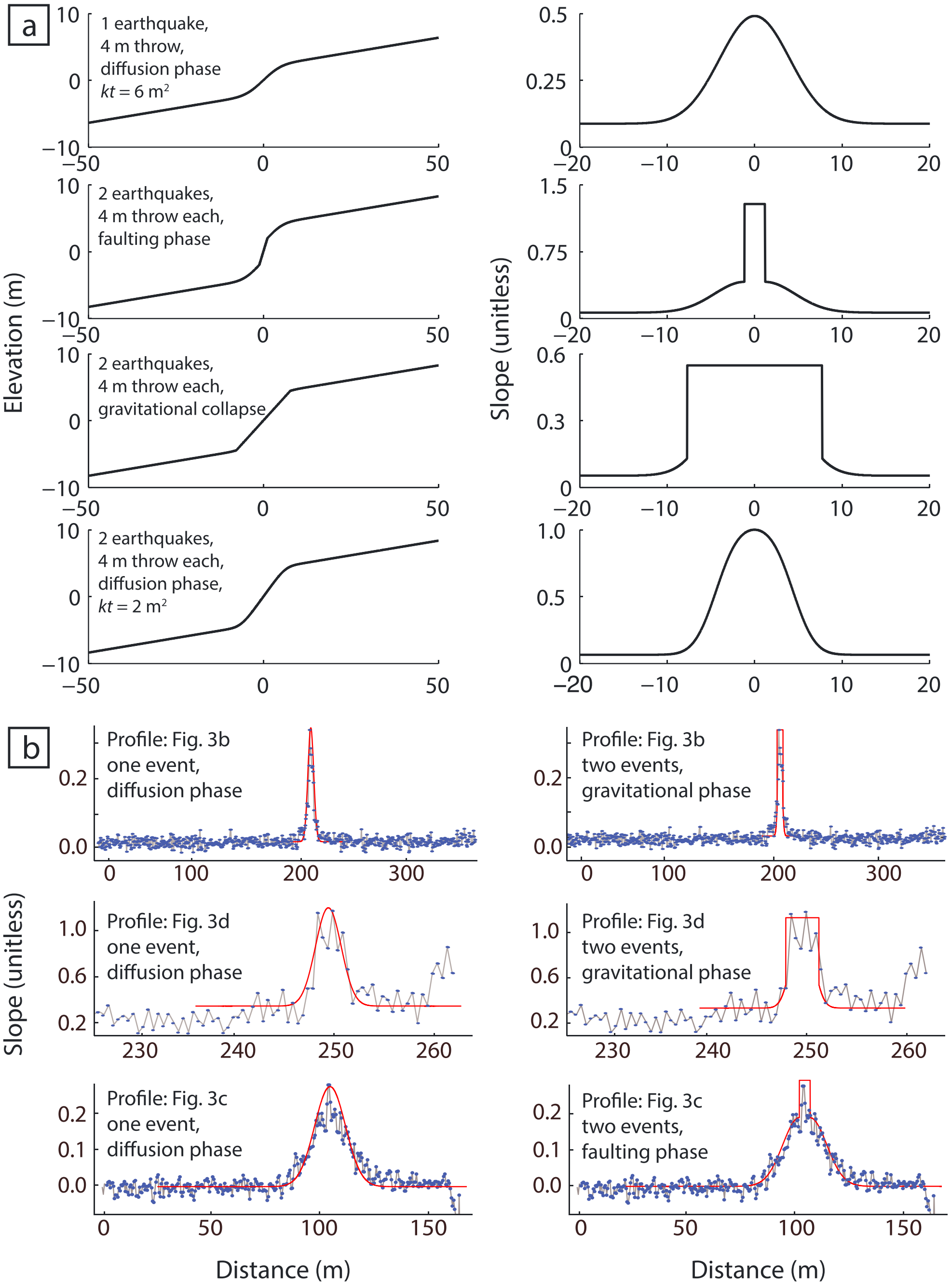

Figure 4. (a) Forward modeled scarp morphology and first derivatives (slope profiles) for one earthquake during the diffusion phase, and two earthquakes in the faulting, gravitational collapses, and diffusion phases based on Avouac and Peltzer (1993). Fault dip of 70° is used for all dislocations, and a 35° angle of repose. The two-earthquake diffusion phase profile assumes that gravitational collapse essentially eliminates the curvature from the prior event. (b) Scarp profile derivatives applied to a three sample profiles in Figure 3. For each profile, we show that topographic scattering prevents us from solving for scarp morphology formed from a unique sequence of processes, and the derivative points can be fit to multiple forward models.

unfiltered vegetation while preserving the overall morphology of the scarp. We also confirm, through testing, that along-strike changes in scarp topography are negligible across the narrow 3 m swath aperture. Each profile length is adjusted upward from an initial 10 m until long enough (up to ~200 m) that readily identifiable *far-field* linear slopes are captured, giving the profiles the general form shown in Figure 3a. In many places, a small hangingwall depression or graben is preserved at the toe of the scarp, the remnants of fissuring caused by fault steepening in the near-surface (Witkind, 1964). Rarely we observe a small free face exceeding the angle of repose (~40°) preserved high up the scarp face, but eroded back from the original free face (Kogan & Bendick, 2011; Wallace, 1980). We look for evidence of composite scarps in the profiles and their derivatives, checking for the characteristic shapes outlined in Figure 4a, but rarely observing clear evidence of them.

To determine the vertical separation, we first manually delimit the observed far-field hangingwall and footwall slopes. Straight lines fit through these slopes, with dip angles b_1 and b_2 on Figure 3, are projected to the scarp center point, also defined manually, where the vertical separation A is then computed. We subsequently estimate the fault throw (the vertical component of fault slip) by combining the *raw* vertical separation and far-field slope measurements with a realistic range of fault dip angles (e.g., Baljinnyam et al., 1993; Thompson et al., 2002). By reporting throw, we can more simply compare with Witkind's (1964) data set, this having been easily measured from the pristine fault free face immediately following the earthquake. We exploit the geometric relationship shown in Figure 3a (modified from Baljinnyam et al., 1993) between vertical separation A, the averaged surface slope angles b_1 and b_2, and the assumed fault dip δ. Based on Witkind's (1964) reported measurements from the freshly exposed fault plane, we use a dip of 70° to compute a preferred fault throw. We also produce an uncertainty range using minimum and maximum dips of 50° and 90°; the minimum value of throw (for dip = 90°) is thus equal to the vertical separation. In choosing this range, we account for the moderate (~10°) change in dip inferred from field observations (section 2.2). The low end of the range is also broadly consistent with dips of 42°–60° determined by seismology and geodesy (section 2.4), though these characterize the earthquake at the scale of the entire seismogenic layer.

For profiles where far-field slopes are unequal, the vertical separation measurement—and thus the computed throw—is sensitive to the placement of the scarp center point (Figure 3a). Thus, we assign each measurement a *quality rating* based on the difference in hangingwall and footwall surface slopes b_1 and b_2. While ideally $b_1 = b_2$, we find that by including measurements at locations where these angles differ—typically those locations where the rupture most closely coincides with the colluvium-bedrock contact—we are able to increase our measurement density and fill in some data gaps, while still capturing the true vertical displacement with reasonable confidence. We thereby assign measurements a high quality rating where the two b values are within 5° of one another, and a poor quality rating where they deviate by >5°. However, even in the latter case, we determine that the uncertainty in throw arising from varying the scarp center point location is much smaller than that which arises from applying the range of fault dips.

Although we inspected profiles along the entire rupture length, the throw distribution has gaps where a scarp is visible but where the vertical separation is below the resolution of the topographic profile. This occurs where the vertical separation is less than ~0.3 m, and where hummocky topography prevents us from defining footwall and/or hangingwall slopes. In such localities, we avoid adding zero-throw points to our distribution so as not to bias subsequent numerical analyses.

In addition to the measurement sensitivities listed above, we acknowledge two other limitations. First, vertical separation measurements may be biased by the effects of lateral slip and local slope azimuth (e.g., Mackenzie & Elliott, 2017). However, scarp free-face striations measured during field mapping showed no significant strike-slip component (Witkind, 1964), nor did we observe any clear lateral offsets during our own analysis. Given that most of our profiles run approximately parallel with the local slope facing direction, such biasing is small. Second, the profiling cannot discriminate between single-event (1959) and composite scarps if the bevel formed in the penultimate event has been removed by erosion, as is observed at the Section 31 trench site (Figure 2a; Hecker et al., 2002; Schwartz et al., 2009) or is obscured by nonplanar far-field slopes. Across the steep colluvium and talus slopes that characterize much of the rupture—especially along the Red Canyon fault ridge section—older scarps may have been removed by erosion before the 1959 earthquake, and so the profiling likely captures only this latest event. However, along parts of the Hebgen and southeastern Red Canyon faults—where bevels were observed during initial mapping of the 1959 earthquake, or can even be seen in pre-1959 aerial photographs (Myers & Hamilton, 1964)—we are aware that profiling may define the cumulative throw of two, or more, earthquakes.

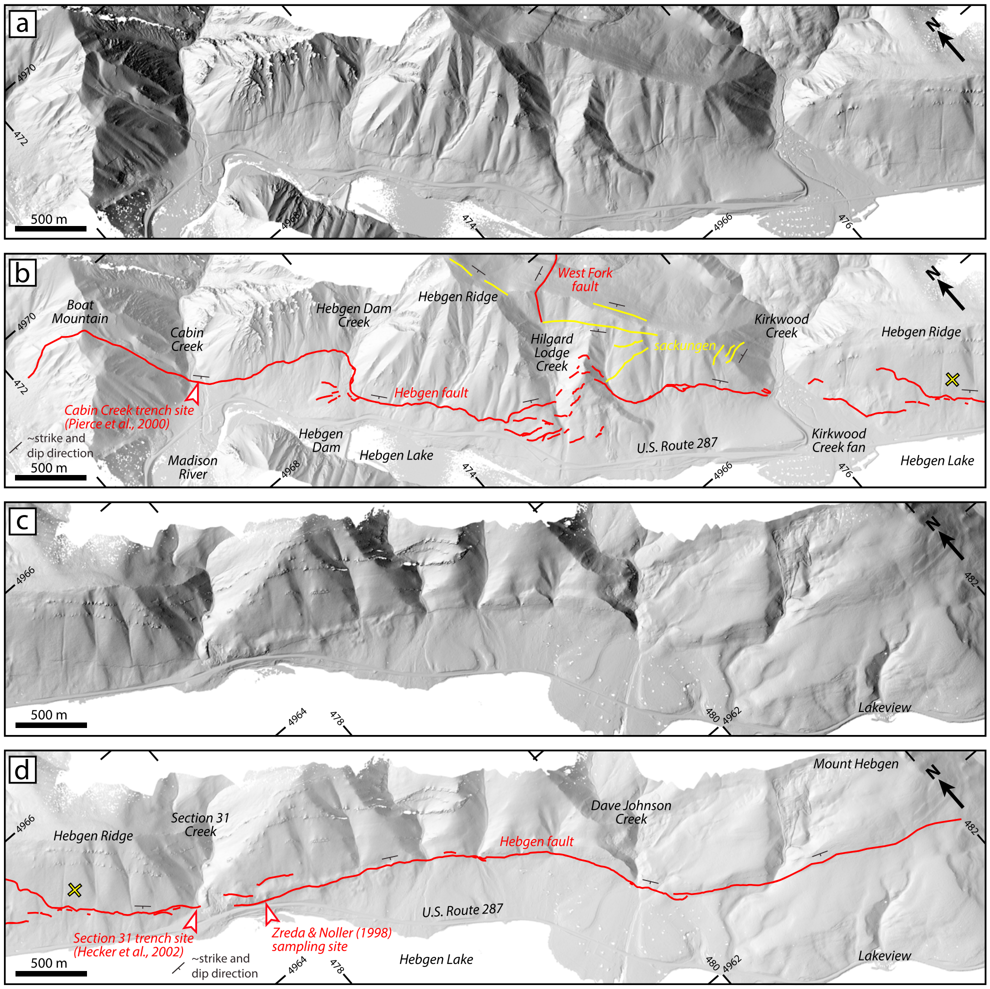

Figure 5. Surface trace of the Hebgen fault rupture. (a) and (b) show the northwestern half of the rupture, without and with annotations, and (c) and (d) similarly show the southeastern half. The yellow cross in (b) and (d) is located at a point common to the two subplot areas. Locations of paleoseismic trench and fault plane exposure dating sites (Hecker et al., 2002; Pierce et al., 2000; Zreda & Noller, 1998) are approximate.

3.3. Subsurface Fault Geometry

We originally hoped to also estimate fault dip by fitting planes to the 3-D surface trace of the 1959 rupture—where the shallow fault plane intersects the surface topography—as in the triple point problem (e.g., Bruhn et al., 1991). Following the procedure of Zhou et al. (2016), we tried a range of along-strike apertures from 50 to 1,000 m. Whatever the aperture used, the orientation of best-fit planes changes drastically along strike (by 10s of degrees over length scales of 100s of meters), such that a robust estimate of fault dip is impossible. We conclude that in the shallow subsurface, the Hebgen and Red Canyon faults are nonplanar over decameter-to-kilometer length scales, whether because of curvature, corrugation, or segmentation. The complete analysis is included in the supporting information.

4. Results and Initial Interpretations

We map a total of ~55 km of surface scarps including splays, multistranded rupture lengths, and antithetic structures, of which ~43 km is characterized as primary surface rupture (Figure 2a). Detailed views of the surface rupture along the Hebgen fault and the Ridge and Southeastern sections of the Red Canyon fault are shown in Figures 5, 6, and 7, respectively. The rupture coordinates are provided as a Google Earth KMZ and an Arc Map shapefile in the supporting information. Scarp profiling yielded 624 vertical separation measurements and coupled throw estimates including 518 at the higher quality rating, thus building substantially upon the ~60 presented by Witkind (1964; Figures 8 and S4–S6).

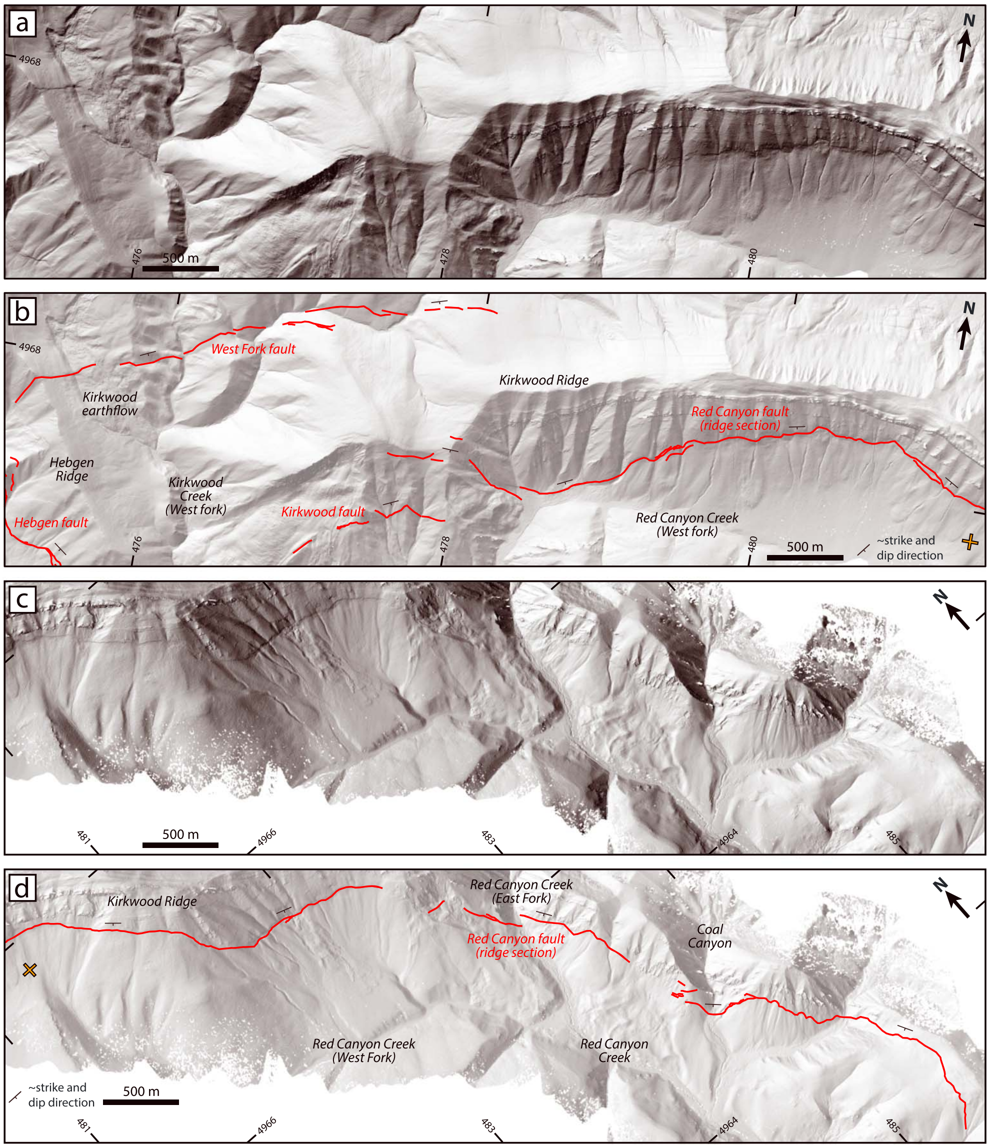

Figure 6. Surface rupture trace along the ridge section of the Red Canyon fault. (a) and (b) show the northwestern half of the rupture, without and with annotations, and (c) and (d) similarly show the southeastern half. The orange cross in (b) and (d) is located at a point common to the two subplot areas.

4.1. Hebgen Fault

Our lidar mapping reveals small-scale structural features of the ~14 km long Hebgen fault rupture (Figure 5), including several bends, breaks, and step overs that were missing from Witkind's (1964) coaser-resolution original map. Two prominent zones of distributed fracturing are identified; the first at Hebgen Dam Creek is associated with a sharp bend in the rupture trace, and the second at Hilgard Lodge Creek coincides with a left-step across a bedrock ridge. High up on the adjacent Hebgen Ridge, we document several uphill-facing scarps which we interpret as sackungen (yellow lines in Figure 5). These appear fresh and so may have formed or been reactivated in the 1959 earthquake.

There are a few notable gaps in the rupture trace. At Kirkwood Creek, the scarp disappears for ~300 m where the projected fault trace crosses a small alluvial fan. However, one of Witkind's throw measurements is located on this same fan, and so the gap probably reflects loss or modification of the scarp through river erosion or residential development rather than being an original characteristic of the rupture. Approximately 1 km southeast of Kirkwood Creek, the scarp takes an ~400 m left-step with some associated fracturing, and there

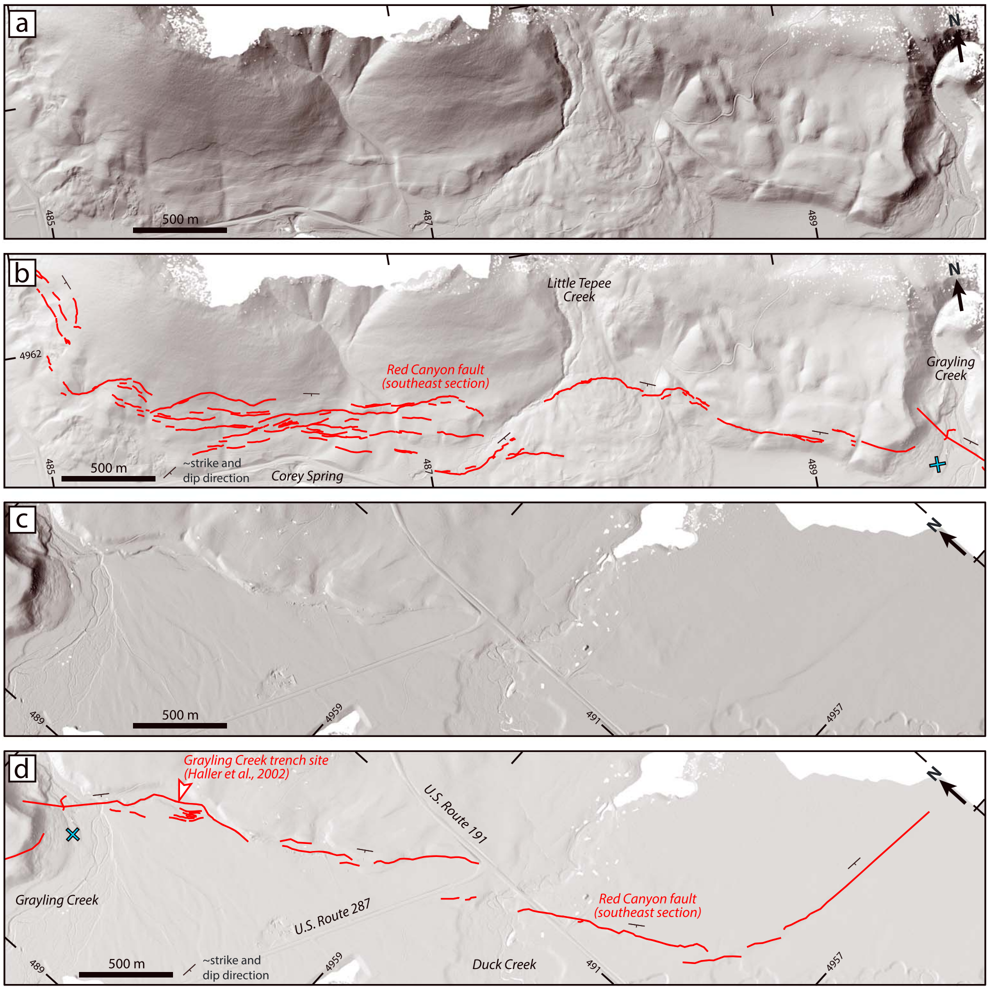

Figure 7. Surface rupture trace along the southeastern section of the Red Canyon fault. (a) and (b) show the northwestern half of the rupture, without and with annotations, and (c) and (d) similarly show the southeastern half. The blue cross in (b) and (d) is located at a point common to the two subplot areas. Location of the (Haller et al., 2002) paleoseismic trench site is approximate.

is a shorter ~200 m gap in the surface trace south of Section 31 Creek. These latter locations are genuine breaks in the surface rupture that are missing from Witkind's map.

Throw estimates along the Hebgen fault scarp are shown in Figure 8a. The majority, colored red in Figure 8a, bracket Witkind's sparser original field measurements but with significant (up to ~2 m) short-wavelength (100s of meters) scatter which is quite typical of well-documented modern earthquakes (e.g., Dolan & Haravitch, 2014; Milliner et al., 2015; Nissen et al., 2014). However, in certain areas, we obtain significantly larger values, too large to be explained by differences in measurement approach (e.g., at Hebgen Dam Creek and NW of Kirkwood Creek, where our typical > ~5 and peak ~8.5 m throw estimates far exceed Witkind's ~1–3 m). Often, the larger values form distinct populations, as defined by near-consecutive data points along a consistent trend with little or no overlap in uncertainty with the smaller values bracketing Witkind's slip profile. A clear example is SE of Dave Johnson Creek, where our throw estimates form two distinct populations at ~1–2 m and ~3–6 m: the lower estimates (colored red in Figure 8a) bracket Witkind's original slip profile, but the higher estimates (colored blue) must represent places where the scarp preserves the cumulative slip of multiple earthquakes.

Considering only those throw estimates that likely capture the 1959 earthquake alone (i.e., those colored red in Figure 8a), we determine average and maximum vertical slip of ~2.3 and ~6.8 m along the Hebgen fault in the 1959 earthquake (Figure 9a). The corresponding values for vertical separation (raw measurements with no correction for fault dip and slope angle) are ~1.9 and ~5.8 m (Figure 9b).

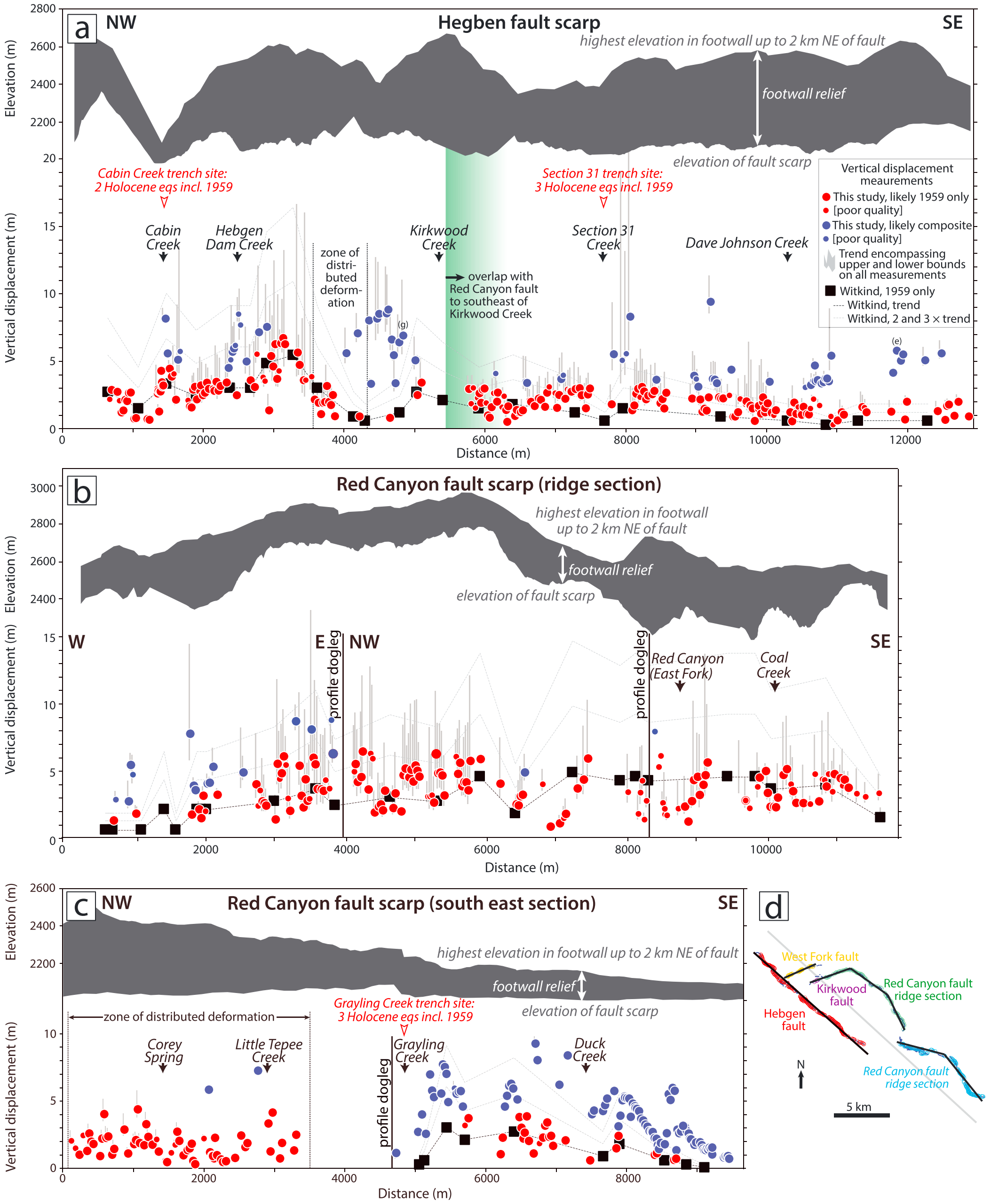

Figure 8. Vertical slip distribution along the 1959 earthquake scarps from our own topographic profiling (colored circles with gray error bars capturing the uncertainty in fault dip) and from Witkind's (1964) field measurements made using *crude geological methods* (black squares), for (a) the Hebgen fault, (b) the Red Canyon fault ridge section, and (c) the Red Canyon fault southeast section. Red circles show vertical slip likely due to only the 1959 earthquake; blue circles show probably composite vertical displacements. The large gray profiles at the top of each panel show relief in the fault footwall. (d) Projection lines and profile measurement data points in map view. Profile center points overlain on the lidar are included in the supporting information.

4.2. Red Canyon Fault, Ridge Section

Our lidar mapping of the ~15 km ridge section of the Red Canyon fault (Figure 6) reveals some rupture details that were not apparent in Witkind's (1964) summary map. The Kirkwood fault lies immediately along strike to the northwest, and so we discuss them together. We observe a few gaps and step overs in the scarp trace at the far northwestern end of the scarp, and again either side of the East Fork of Red Canyon Creek, that are missing from Witkind's map. However, these steep slopes are prone to landsliding and so we cannot rule out that the scarp has been removed through mass wasting. Along Kirkwood Ridge, we also observe a few

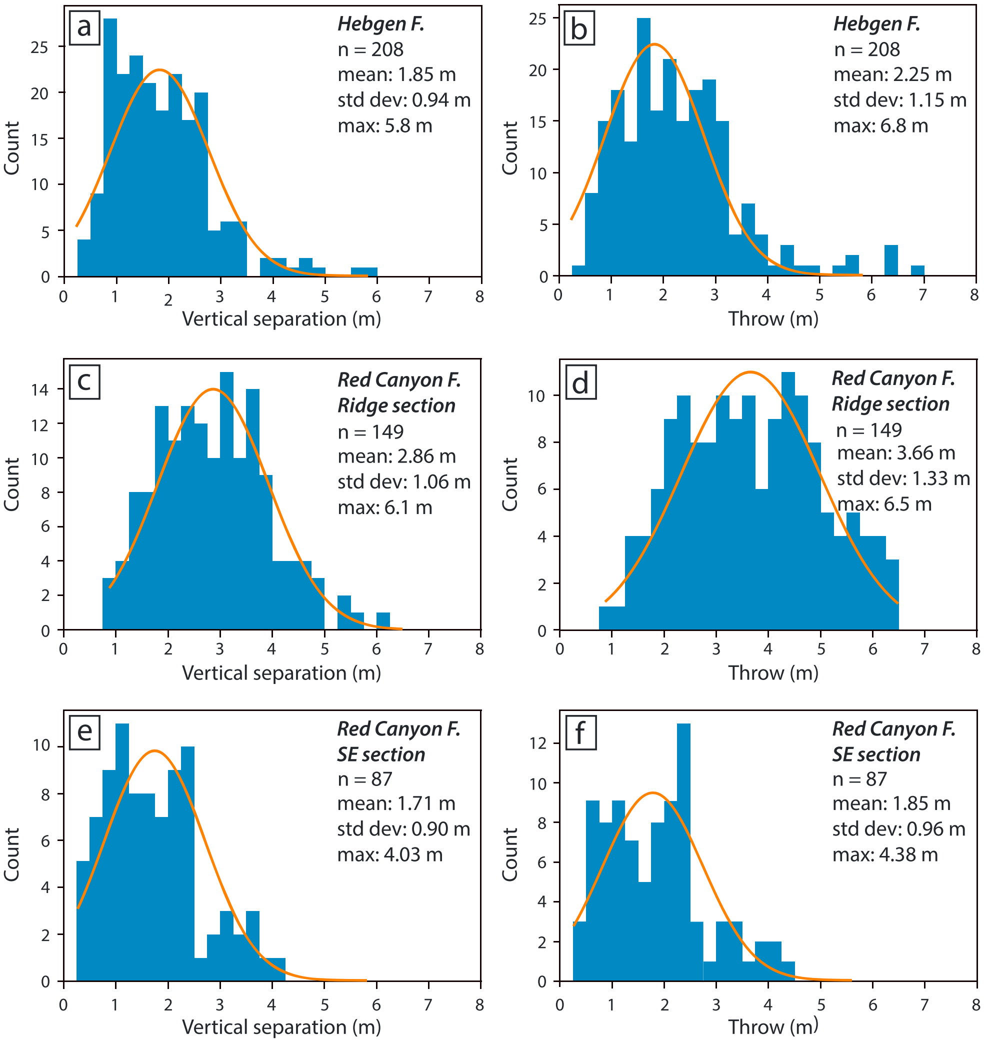

Figure 9. Vertical separation (left column) and throw (right column) in the 1959 Hebgen Lake earthquake along the (a, b) Hebgen, (c, d) Red Canyon ridge, and (e, f) Red Canyon southeast faults. Only data deemed as representing a single event are included (red-colored points in Figure 8). Bins are 0.25 m, and standard deviations are calculated from the normalized distributions shown in orange. Across all three faults, the average vertical separation is 2.16 m and the average throw 2.64 m.

short, parallel fractures and localized scarp bifurcations separated by only 10s of meters. We find no evidence to support the suggestion by Hart et al. (2012) that the Red Canyon scarp represents a landslide headwall. Within the lidar coverage, we find no compressive thrust scarps or folds that could indicate the toe of such a landslide. We are also able to trace the scarp continuously across the floor of Coal Canyon (Figures 6c–6d), which seems inconsistent with a landsliding origin.

Estimating throw along the ridge section of the Red Canyon fault was challenging. The footwall far-field slope (b_2) is often steeper than that of the hangingwall (b_1) by several degrees, so our throw distribution incorporates vertical separation measurements from many poor quality profiles. Furthermore, the scarp cuts steep slopes, so the choice of scarp free-face dip has a large impact on the computed throw. These limitations may contribute to the much higher level of scatter we observe in our throw profile compared to Witkind's (Figure 8b), but our displacements do generally bracket the 1959 values, and where the datapoints are colocated they are mostly in close agreement. We do not observe clear separation of the throw estimates into distinct populations as we earlier described for the Hebgen fault. We instead tentatively assign multievent status to the largest estimates that, accounting for uncertainties, double or more than double Witkind's nearest original measurements; most of these are along the northwest part of the fault.

Considering only the likely single-event throw estimates (those colored red in Figure 8b), we determine average and maximum vertical slip of ~3.7 and ~6.5 m along the Ridge section of the Red Canyon fault in the 1959 earthquake (Figure 9c). The corresponding values for vertical separation are ~2.9 and ~6.1 m (Figure 9d).

4.3. Red Canyon Fault, Southeast Section

The ~10 km long southeast section of the Red Canyon fault has the most complex rupture trace of the three major 1959 rupture strands (Figure 7). This complexity is apparent in the original field reports and Witkind's (1964) map, but the lidar data provide additional detail. Northwest of Little Tepee Creek, the rupture comprises a diffuse fracture zone up to ~400 m wide. Here the surface deformation pattern is likely influenced by closely spaced bedding planes of the underlying Paleozoic sediments, and the rupture mimics changes in bedrock strike as it takes a ~90° bend from Red Canyon onto the rangefront at Corey Spring (Witkind et al., 1964). Southeast of Little Tepee Creek, the rupture is mostly single-stranded but remains highly discontinuous, with individual strands sections no more than ~1 km in length separated by several gaps and step overs of up to ~200 m.

Throw estimates along the scarps of the southeast Red Canyon fault section are shown in Figure 8c. Northwest of Little Tepee Creek, we are able to assess throw along a dominant, SW-facing scarp, with clustering in the ~1–3 m range. Witkind (1964) described this section qualitatively but did not report slip, and so we cannot easily ascertain whether this section of scarp captures only the 1959 earthquake or also preceding events in some spots. We tentatively mark two gross outliers (>5 m) as multievent. Southeast of Grayling Creek, many of our throw estimates greatly exceed Witkind's 1959 scarp heights often by two to three times, and must therefore capture multiple earthquakes, while our lowest throw estimates are in close agreement with the nearest of Witkind's. This fault section displaces a planar and subhorizontal surface, such that the raw vertical separation measurements have low uncertainty, the derived throw estimates are only minimally affected by the range in fault dip, and our throw estimates vary smoothly along continuous rupture strands. Thus, we confidently assign throw estimates that more than double Witkind's nearest measurements as multievent.

Considering only the likely single-event throw estimates (those colored red in Figure 9c), we determine average and maximum vertical slip of ~1.9 and ~4.4 m along the southeastern section of the Red Canyon fault in the 1959 earthquake (Figure 9e). The corresponding values for vertical separation are ~1.7 and ~4.0 m (Figure 9f).

5. Discussion

5.1. 1959 Earthquake Slip Distribution

We now discuss the distribution of vertical slip estimates attributed to the 1959 earthquake alone, plotted in red in Figure 8, in the context of the kilometer-scale fault structure and rupture characteristics. We surmise that the cumulative (long-term) vertical slip on the fault is roughly proportional to the relief of the footwall block, characterized in Figure 8 as the elevation difference between the scarp and the highest point in the immediate footwall (up to 2 km perpendicular to the scarp). Thus, the Hebgen fault, with typical footwall relief of ~300–600 m, is structurally more mature (has more cumulative slip) than the Red Canyon fault, with an equivalent range of ~100–400 m. As noted by Perrin et al. (2016), the Red Canyon fault appears to be propagating eastward into the West Yellowstone Basin, where footwall relief gradually diminishes to zero. However, we are cautious not to over interpret the footwall relief since (1) some of the topography is likely antecedent to modern normal faulting, inherited instead from Laramide thrust faulting and folding, and (2) in a few places, most notably at Cabin Creek, deep canyons are cut into the footwall that may not correspond with low-cumulative slip sections of the fault.

In Figure 10, we project 1959 throw from the Red Canyon and Hebgen faults onto a single strike. Given the likelihood that the two faults merge at depth (Doser, 1985), we also calculate the summed throw, which averages 3.6 ± 2.0 m and peaks at ~9.2 m. The depletion of slip along the eastern Hebgen fault is compensated by slip on the Red Canyon fault, such that peak cumulative slip is located approximately centrally to the overall rupture length, adjacent to an area of high footwall relief on the Hebgen fault. The largest cumulative coseismic slip is therefore associated with the most structurally mature part of the fault system, conforming with a pattern that is widespread among large earthquakes (Perrin et al., 2016).

Equally, many of the low points in the 1959 slip distribution correspond with structural features that likely influenced rupture propagation. For example, vertical slip on the Hebgen fault decreases to <1 m SE of Hilgard

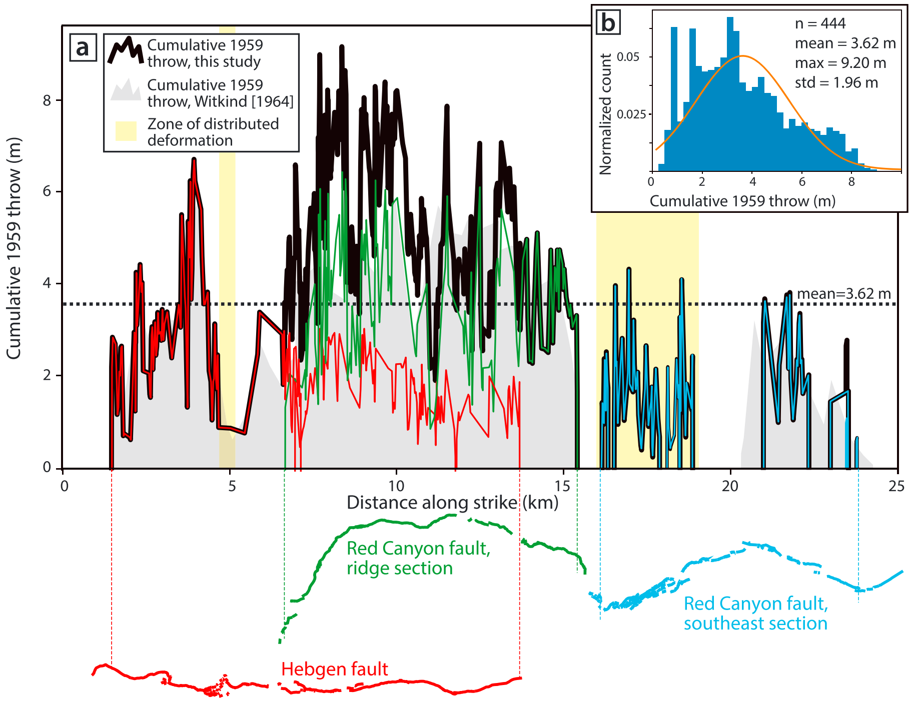

Figure 10. (a) Cumulative along-strike 1959 throw, from projecting single-event vertical slip measurements (red datapoints in Figure 8) onto the simplified fault trend shown in Figure 8d to adding interpolated trends for the Hebgen and Red Canyon faults where they overlap. Individual Hebgen fault, Red Canyon ridge, and Red Canyon southeast throws are plotted in red, green, and blue, respectively, with zero-throw points appended to the endpoints of each. Vertical dashed lines correlate the fault section endpoints with the mapped surface rupture below the plot. The cumulative throw is the thick black line, with a mean value of 3.62 m (horizontal dashed line). The gray polygon is Witkind's cumulated throw measurements, summed and projected in the same manner. (b) Cumulative throw in the 1959 Hebgen Lake earthquake in 0.25 m bins. The standard deviation (std) is calculated from the normalized distribution shown in orange.

Lodge Creek, which is close to the W end of the West Fork fault (Figure 8a). Similarly, the step over S of Kirkwood Creek—another low point in the throw distribution—is where the Kirkwood fault approaches the Hebgen fault, identified as a possible barrier to rupture by Manighetti et al. (2005). There are minima in the Red Canyon fault throw distribution where the scarp descends from Kirkwood Ridge into Red Canyon and bends toward the south, at the intersection between the Ridge and Southeastern sections, and at the bend in fault strike N of Grayling Creek (Figures 8b–8c).

The new vertical slip distribution enables us to estimate the moment magnitude of the 1959 earthquake. We use the equations for seismic moment, M_0, and moment magnitude, M_w (Hanks & Kanamori, 1979):

$$M_0 = \mu A \bar{u}, \tag{1}$$

$$M_w = \frac{2}{3}\left[\log_{10} M_0 - 9.1\right], \tag{2}$$

where μ is the shear modulus (which we fix at 3.2×10^{10} N/m^2), A is fault area (length L × down-dip width W), and $\bar{u}$ is mean slip. We compute a range of moment magnitudes by summing the seismic moment calculated for each of the three major rupture sections and exploring a parameter space that includes the conservative ranges of 10–20 km in fault bottom depth and 40°–60° in the gross fault dip characteristic of this depth scale (see sections 2.3 and 2.4). This yields the range in W of 11.5–31.1 km with a preferred value of 19.6 km. We use the shallow dip range of 50°–90° to convert the average vertical surface slip on each rupture section to $\bar{u}$, computing ranges of 2.3–2.9 m, 3.7–4.8 m, and 1.9–2.4 m over L of 14, 12, and 10.5 km for the Hebgen fault and the ridge and southeast sections of the Red Canyon fault, respectively. The estimated moments range from ~3.0 to 10.3×10^{19} Nm (M_w ~6.9–7.3), with a preferred value of ~5.2×10^{19} Nm (M_w 7.1). This compares favorably with the contemporary USGS/ISC-GEM moment of ~8×10^{19} Nm (Storchak et al., 2015), but greatly exceeds an estimate of M_w 6.9 calculated using the magnitude-surface rupture length regressions of Wells and Coppersmith (1994) and a cumulative rupture length of 36.5 km.

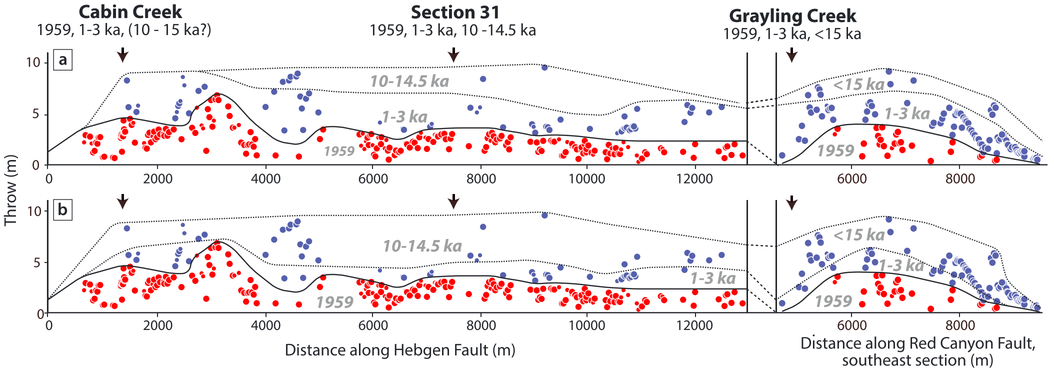

Figure 11. (a) and (b) Two possible smoothed throw distributions for prehistoric earthquakes interpreted with the paleoseismic records (Haller et al., 2002; Hecker et al., 2002; Pierce et al., 2000; Schwartz et al., 2009), with distances as in Figure 8. Throw data attributed to the 1959 earthquake are colored red, and multievent offsets are in blue.

5.2. Latest Pleistocene/Holocene Paleo-Earthquakes

Here we discuss the cumulative vertical displacement data (those offsets formed by multiple events, colored blue in Figure 8). To recap, these slip estimates mostly exceed the Witkind field measurements and adjacent estimates in our own throw distribution by at least double, often forming a distinct population with little overlap in uncertainty. We consider, but rule out, the possibility that differences in measurement times and approaches may have biased our lidar-derived offsets toward larger values. First, while topographic profiling captures more of the off-fault deformation than the original field measurements, this does not explain estimates that in places exceed the 1959 measurements by several times over. At these locations, the profiling must record slip in one or more preceding events, as was reported locally to the Section 31 and Grayling Creek trench sites by Hecker et al. (2002) and Schwartz et al. (2009). Second, while 50 years elapsed between data collections, postseismic geodetic surveys collected immediately after the earthquake and again decades later rule out significant postseismic surface slip along the faults we investigate here (Nishimura & Thatcher, 2003). No recent afterslip has been observed by returning field geologists, and on the contrary, they have reported field and paleoseismic evidence of multiple events (e.g., Kogan & Bendick, 2011; Nash, 1984; Wallace, 1980; Zreda & Noller, 1998).

Unfortunately, we cannot obtain paleo-earthquake slip distributions for the Hebgen and Red Canyon faults in the manner that is often possible for major strike-slip faults (e.g., Haddon et al., 2016; Klinger et al., 2011; Manighetti et al., 2015; Salisbury et al., 2012; Zielke et al., 2012). Scarps formed by vertical slip are prone to rapid degradation and thus have lower preservation potential than laterally offset piercing points. Nevertheless, using preliminary paleoseismic trench results and accompanying field observations as the basis for interpretation (Haller et al., 2002; Hecker et al., 2002; Pierce et al., 2000; Schwartz et al., 2009), we can construct a suite of possible models for the latest Pleistocene–present slip history of the Hebgen and Red Canyon faults; Figure 11 depicts two possible interpretations. We assume that all multievent offsets, most of which cut colluvial or alluvial deposits, are latest Pleistocene or younger. Following Schwartz et al. (2009), we assign a penultimate rupture at ~1–3 ka along the entire Hebgen fault and the southeast section of the Red Canyon fault. We also include a latest Pleistocene–early Holocene earthquake at Section 31 Creek (younger than ~15 ka) and at Grayling Creek (11–14 ka), which may or may not have also ruptured Cabin Creek. The Red Canyon fault ridge section has not been trenched and is not depicted on this plot.

Multievent displacements are preserved intermittently along the Hebgen fault from Cabin Creek to its southeast rupture terminus (Figure 8a). Between Hebgen Dam Creek and Kirkwood Creek, 1959 slip decreases southeastward while multievent scarps show the opposite trend, culminating in a cluster of ~8 m multievent slip estimates that coincide with a low in the 1959 slip distribution. Assuming that sites on either side of Hebgen Dam Creek record the same number of earthquakes, this implies variable displacement per earthquake at this location. East of Kirkwood Creek, cumulative throw estimates reveal throw populations distinguishable from 1959, which may include both penultimate and prepenultimate events (e.g., two ~8–9 m outliers at 8,000–9,500 m along strike far exceed values already assigned multievent; Figure 11). At these locations, one of the earlier Holocene/latest Pleistocene earthquakes may have had several times the slip of the 1959 earthquake, measured locally by Witkind, at <2 m, again implying variable local displacement per event.

Along the Red Canyon fault ridge section, distinguishing single-event and multievent scarps is challenging since our throw estimates do not form distinct populations (Figure 8b). In the west, most of our estimated vertical displacements exceed Witkind's measured values, while in the east, our estimates generally bracket them. The largest of the western displacements (~7 m) are thus considered multievent, though the cut-off between what is 1959 only and what is multievent is unclear. It appears likely that this section has ruptured during the Holocene, but without trench data, we cannot say whether it did so together with the other major fault sections. The scarcity of a multievent signal along the Red Canyon fault ridge section, including its complete absence from the eastern part, may reflect the lower preservation potential of scarps in steep talus slopes, compared to the rangefront-forming Hebgen and southeast Red Canyon faults.

Along the southeast Red Canyon fault, we focus southeast of Grayling Creek where composite scarps are best preserved and throw estimates are well constrained with small uncertainties (Figures 8c and 11). Our throw estimates generally exceed Witkind's and thus capture one or both of the pre-1959 earthquakes known from paleoseismic trenching (Haller et al., 2002). At ~7500–8500 m along strike, our vertical displacement estimates closely follow the ×3 multiple of Witkind's interpolated 1959 trend, and the decrease in both trends toward the southeast mimics that of the footwall relief. This suggests consistency between prehistoric slip gradients and that of the 1959 earthquake in this location at the southeast fault terminus.

Figure 11 shows possible models for the latest Pleistocene–present slip history of the Hebgen fault and Red Canyon fault southeast section, depicting two extreme cases in which the two prehistoric events produced contrasting slip distributions. Both models assume that the fault slip rate is spatially constant, thus projecting the total vertical slip envelope approximately horizontally, through the scattered ~9 m throw maxima. However, we allow slip per earthquake to vary along strike, meeting two criteria: (1) at trench sites, we comply to the paleoseismic interpretations (Haller et al., 2002; Hecker et al., 2002; Pierce et al., 2000; Schwartz et al., 2009); and (2) projecting the penultimate event slip envelope between colocated slip populations. The first model (Figure 11a) attributes more of the preserved vertical slip to the penultimate event, while the second model (Figure 11b) attributes this to the prepenultimate event. The schematics reveal the possibility of earthquakes with approximately half the slip (and thus half the seismic moment) occurring on this fault system, as well as high slip variability among events at each point.

To summarize, slip distributions of two prehistoric earthquakes that ruptured the Hebgen and Red Canyon rangefront faults generally do not mimic that of the 1959 rupture, even if the rupture lengths may be the same, or similar. However, we also acknowledge that while the semiautomated approach employed here facilitates hundreds of discrete scarp height measurements, it is no substitute for forensic, site-specific analysis of the geomorphology, which could yield firm constraints on paleo-earthquake chronologies and long-term slip rates at discrete locations. For example, southeast of Cabin Creek, we observe that the scarp height appears to vary systematically across surfaces of different apparent age, much as Nash (1984) observed along unnamed scarps south of Hebgen Lake. With surface dating, robust earthquake chronologies could be extracted from such sites, supplementing the paleoseismic studies of Haller et al. (2002), Hecker et al. (2002), Pierce et al. (2000), and Schwartz et al. (2009), but doing so lies beyond the scope of this paper.

5.3. Scarp Morphology

The Hebgen fault scarps analyzed in this study generally retain profile morphology that cannot be uniquely modeled as one or two earthquakes (Figure 4). To consider the possibility that our semiautomated profiling approach may have prevented us from detecting any beveled scarps, we manually picked and inspected discrete scarp profiles in between the automatic 30-m spaced profiles, looking specifically in areas where Hecker et al. (2002) and Schwartz et al. (2009) report cumulative scarps. After careful searching, the manual approach does reveal a few short sections of beveled scarp, for example, near Grayling Creek (Figure S1). Nevertheless, the great majority of profiles retain a simple morphology, even in places where cumulative displacements are strongly suspected.

At the Section 31 trench site on the Hebgen fault, photographs from shortly after the 1959 earthquake preserve evidence of an old Holocene scarp from the penultimate event, but this morphology has largely disappeared due to retreat of the 1959 free face (Hecker et al., 2002; Schwartz et al., 2009). Our lidar analysis shows that the removal or masking of degraded paleo-earthquake scarps and bevels—by degradation of the 1959 free face—may be widespread, beyond Section 31. As Hecker et al. (2002) and Schwartz et al. (2009) point out, this observation has important wider implications, cautioning against the practice of assuming that morphologically simple scarps represent a single earthquake rupture. For example, had Witkind's (1964) early field measurements been unavailable, we might have attributed many of the cumulative scarp displacements to a single earthquake, whose moment magnitude would then have been overestimated.

6. Conclusions

New airborne lidar topography data along the multistranded 1959 M_w 7.2 Hebgen earthquake surface rupture reveal details of its slip distribution that were not apparent in original field mapping. Densely spaced topographic profiles indicate that although the now-degraded fault scarp mostly exhibits a simple form, its throw often exceeds that measured at the 1959 fresh scarp free face by twofold or more. Profile-derived throw estimates must, in places, capture one or more latest Pleistocene–Holocene paleo-earthquakes in addition to 1959 slip. This has implications for interpreting simple scarps along faults lacking historical or paleoseismic records. Considered alongside preliminary trench results, populations of single-event and multievent throw estimates indicate that the Hebgen and Red Canyon faults rupture with variable local slip-per-event.

Acknowledgments

Lidar measurements were acquired and processed by the National Center for Airborne Laser Mapping (NCALM) through a Seed Grant to KLJ, and we thank all of those involved in producing this outstanding data set. NCALM is funded by the National Science Foundation (NSF) Division of Earth Sciences, Instrumentation and Facilities Program through Award Number 1043051. The data are now hosted at OpenTopography (http:// opentopo.sdsc.edu/datasetMetadata?otCollectionID=OT.052016.26912.1; https://doi.org/10.5069/G9H41PCJ), funded under NSF Award Numbers 1226353 and 1225810. We have been supported through the duration of this project by the Southern California Earthquake Center (SCEC), through Award Numbers 14101 and 15189; by NSF, through Award Numbers 1461574 and 1524815; by a grant from the Newmont Mining Corporation; and by the Natural Sciences and Engineering Research Council of Canada (NSERC), through Discovery Grant Number 2017-04029. There are no conflicts of interests, financial or otherwise, for any of the authors or either of their affiliations. We are grateful to Warren Hamilton, Rebecca Bendick, Dylan Schmeelk, Ramon Arrowsmith, Mike Oskin, Ryan Gold, Gavin Hayes, Paul Sava, Wendy Zhou, and Chris Duross for thought-provoking conversations on this earthquake and to Megan Gallagher and Joseph Halloran for their assistance on a short field trip to the Hebgen region. Finally, we would like to thank associate editor Isabelle Manighetti, David Schwartz, and three anonymous reviewers for their comments which greatly improved the manuscript.

References

Avouac, J. P., & Peltzer, G. (1993). Active tectonics in southern Xinjiang, China: Analysis of terrace riser and normal fault scarp degradation along the Hotan-Qira fault system. *Journal of Geophysical Research*, *98*(B12), 21,773–21,807.

Baljinnyam, I., Bayasgalan, A., Borisov, B. A., Cisternas, A., Dem'yanovich, M. G., Ganbaatar, L., et al. (1993). Ruptures of major earthquakes and active deformation in Mongolia and its surroundings. *Geological Society of America Memoirs*, *181*, 1–62.

Barrientos, S. E., Stein, R. S., & Ward, S. N. (1987). Comparison of the 1959 Hebgen Lake, Montana and the 1983 Borah Peak, Idaho, earthquakes from geodetic observations. *Bulletin of the Seismological Society of America*, *77*(3), 784–808.

Benedetti, L., Manighetti, I., Gaudemer, Y., Finkel, R., Malavieille, J., Pou, K., et al. (2013). Earthquake synchrony and clustering on Fucino faults (Central Italy) as revealed from in situ ^{36}Cl exposure dating. *Journal of Geophysical Research: Solid Earth*, *118*, 4948–4974. https://doi.org/10.1002/jgrb.50299

Bruhn, R. L., Yang, Z., Wu, D., & Yonkee, W. A. (1991). Structure of the warm spring and northern Thousand Springs fault segments, lost river fault zone, Idaho: Possible effects on rupturing during the 1983 Borah Peak earthquake. *Tectonophys*, *200*(1), 33–49.

Chen, Y.-G., Chen, W.-S., Lee, J.-C., Lee, Y.-H., Lee, C.-T., Chang, H.-C., & Lo, C.-H. (2001). Surface rupture of 1999 Chi-Chi earthquake yields insights on active tectonics of central Taiwan. *Bulletin of the Seismological Society of America*, *91*(5), 977–985.

Dolan, J. F., & Haravitch, B. D. (2014). How well do surface slip measurements track slip at depth in large strike-slip earthquakes? The importance of fault structural maturity in controlling on-fault slip versus off-fault surface deformation. *Earth and Planetary Science Letters*, *388*, 38–47.

Doser, D. I. (1985). Source parameters and faulting processes of the 1959 Hebgen Lake, Montana, earthquake sequence. *Journal of Geophysical Research*, *90*, 4537–4555.

Elliott, A. J., Dolan, J. F., & Oglesby, D. D. (2009). Evidence from coseismic slip gradients for dynamic control on rupture propagation and arrest through stepovers. *Journal Geophysical Research*, *114*, B02313. https://doi.org/10.1029/2008JB005969

Fletcher, J. M., Teran, O. J., Rockwell, T. K., Oskin, M. E., Hudnut, K. W., Mueller, K. J., et al. (2014). Assembly of a large earthquake from a complex fault system: Surface rupture kinematics of the 4 April 2010 El Mayor–Cucapah (Mexico) Mw 7.2 earthquake. *Geosphere*, *10*(4), 797–827.

Fraser, G. D. (1964). Intensity, magnitude, and ground breakage, *The Hebgen Lake, Montana, Earthquake of August 17, 1959* (Vol. 435, pp. 31–35), Geological Survey Professional Paper. Washington: U.S. Government Printing Office.

Haddon, E. K., Amos, C. B., Zielke, O., Jayko, A. S., & Bürgmann, R. (2016). Surface slip during large Owens Valley earthquakes. *Geochemistry, Geophysics, Geosystems*, *17*, 2239–2269. https://doi.org/10.1002/2015GC006033

Haller, K. M., Machette, M. N., Dart, R. L., & Rhea, B. S. (2004). US Quaternary fault and fold database released. *Eos, Transactions of the American Geophysical Union*, *85*(22), 218–218.

Haller, K. M., Tsutsumi, H., Machette, M. N., Essex, J., & Hancock, D. (2002). Paleoseismic investigation of the 1959 Red Canyon fault, southwestern Montana. *Geological Society of America Abstracts with Programs*, *34*, A–4. https://gsa.confex.com/gsa/2002RM/webprogram/Paper33924.html

Hamling, I. J., Hreinsdóttir, S., Clark, K., Elliott, J., Liang, C., Fielding, E., et al. (2017). Complex multifault rupture during the 2016 Mw 7.8 Kaikoura earthquake, New Zealand. *Science*, *356*(6334), eaam7194.

Hanks, T., & Kanamori, H. (1979). A moment magnitude scale. *Journal of Geophysical Research*, *84*, 2348–2351.

Hart, M. W., Shaller, P. J., & Farrand, G. T. (2012). When landslides are misinterpreted as faults: Case studies from the western United States. *Environmental and Engineering Geoscience*, *18*(4), 313–325.

Hecker, S., Stenner, H. D., Costa, C. H., Schwartz, D. P., & Hamilton, J. C. (2002). New paleoseismic results from the central part of the 1959 Hebgen fault rupture, Montana. *Geological Society of America Abstracts with Programs*, *34*, A–4. https://gsa.confex.com/gsa/2002RM/webprogram/Paper34254.html

Hollingsworth, J., Leprince, S., Ayoub, F., & Avouac, J.-P. (2012). Deformation during the 1975-1984 Krafla rifting crisis, NE Iceland, measured from historical optical imagery. *Journal of Geophysical Research*, *117*, B11407. https://doi.org/10.1029/2012JB009140

Kaneda, H., Nakata, T., Tsutsumi, H., Kondo, H., Sugito, N., Awata, Y., et al. (2008). Surface rupture of the 2005 Kashmir, Pakistan, earthquake and its active tectonic implications. *Bulletin of the Seismological Society of America*, *98*, 521–557.

Klinger, Y., Etchebes, M., Tapponnier, P., & Narteau, C. (2011). Characteristic slip for five great earthquakes along the Fuyun fault in China. *Nature Geoscience*, *4*, 389–392.

Kogan, L., & Bendick, R. (2011). A mass failure model for the initial degradation of fault scarps, with application to the 1959 scarps at Hebgen Lake, Montana. *Bulletin of the Seismological Society of America*, *101*, 68–78.

Leprince, S., Berthier, E., Ayoub, F., Delacourt, C., & Avouac, J.-P. (2008). Monitoring Earth surface dynamics with optical imagery. *Eos, Transactions of the American Geophysical Union*, *89*, 1–2.

Mackenzie, D., & Elliott, A. (2017). Untangling tectonic slip from the potentially misleading effects of landform geometry. *Geosphere*, *13*(4), 1310–1328.

Manighetti, I., Campillo, M., Sammis, C., Mai, P. M., & King, G. (2005). Evidence for self-similar, triangular slip distributions on earthquakes: Implications for earthquake and fault mechanics. *Journal of Geophysical Research*, *110*, B05302. https://doi.org/10.1029/2004JB003174

Manighetti, I., Perrin, C., Dominguez, S., Garambois, S., Gaudemer, Y., Malavieille, J., et al. (2015). Recovering paleoearthquake slip record in a highly dynamic alluvial and tectonic region (Hope Fault, New Zealand) from airborne lidar. *Journal of Geophysical Research: Solid Earth*, *120*, 4484–4509. https://doi.org/10.1002/2014JB011787

Milliner, C. W. D., Dolan, J. F., Hollingsworth, J., Leprince, S., Ayoub, F., & Sammis, C. G. (2015). Quantifying near-field and off-fault deformation patterns of the 1992 M_W 7.3 Landers earthquake. *Geochemistry, Geophysics, Geosystems*, *16*, 1577–1598. https://doi.org/10.1002/2014GC005693

Murphy, L. M., & Brazee, R. J. (1964). Seismological investigations of the Hebgen Lake earthquake, *The Hebgen Lake, Montana, Earthquake of August 17, 1959* (Vol. 435, pp. 13–17), Geological Survey Professional Paper. Washington: U.S. Government Printing Office.

Myers, W. B., & Hamilton, W. (1964). Deformation accompanying the Hebgen Lake earthquake of August 17, 1959, *The Hebgen Lake, Montana, Earthquake of August 17, 1959* (Vol. 435, pp. 55–98), Geological Survey Professional Paper. Washington: U.S. Government Printing Office.

Nash, D. B. (1984). Morphologic dating of fluvial terrace scarps and fault scarps near West Yellowstone, Montana. *Geological Society of America Bulletin*, *95*(12), 1413–1424.

Nishimura, T., & Thatcher, W. (2003). Rheology of the lithosphere inferred from postseismic uplift following the 1959 Hebgen Lake earthquake. *Journal of Geophysical Research*, *108*(B8), 2389. https://doi.org/10.1029/2002JB002191

Nissen, E., Elliott, J. R., Sloan, R. A., Craig, T. J., Funning, G. J., Hutko, A., et al. (2016). Limitations of rupture forecasting exposed by instantaneously triggered earthquake doublet. *Nature Geoscience*, *9*, 330–336.

Nissen, E., Maruyama, T., Ramon Arrowsmith, J., Elliott, J. R., Krishnan, A. K., Oskin, M. E., & Saripalli, S. (2014). Coseismic fault zone deformation revealed with differential lidar: Examples from Japanese M_W ~7 intraplate earthquakes. *Earth and Planetary Science Letters*, *405*, 244–256.

Oskin, M. E., Arrowsmith, J. R., Corona, A. H., Elliott, A. J., Fletcher, J. M., Fielding, E. J., et al. (2012). Near-field deformation from the El Mayor-Cucapah earthquake revealed by Differential LIDAR. *Science*, *335*, 702–705.

Payne, S. J., McCaffrey, R., King, R. W., & Kattenhorn, S. A. (2012). A new interpretation of deformation rates in the Snake River Plain and adjacent basin and range regions based on GPS measurements. *Geophysical Journal International*, *189*, 101–122.

Perrin, C., Manighetti, I., Ampuero, J. P., Cappa, F., & Gaudemer, Y. (2016). Location of largest earthquake slip and fast rupture controlled by along-strike change in fault structural maturity due to fault growth. *Journal of Geophysical Research: Solid Earth*, *121*, 3666–3685. https://doi.org/10.1002/2015JB012671

Pierce, K. L., Lageson, D. R., Ruleman, C. A., & Hintz, R. G. (2000). Paleoseismology of Hebgen Lake normal fault at Cabin Creek, MT; Preliminary report of the Hebgen Lake Paleoseismology Working Group. *Geological Society of America Abstracts with Programs*, *32*(4), 442.

Ryall, A. (1962). The Hebgen Lake, Montana, earthquake of August 18 1959: P waves. *Bulletin of the Seismological Society of America*, *52*(2), 235–271.

Salisbury, J. B., Rockwell, T. K., Middleton, T. J., & Hudnut, K. W. (2012). LiDAR and field observations of slip distribution for the most recent surface ruptures along the central San Jacinto fault. *Bulletin of the Seismological Society of America*, *102*(2), 598–619.

Schmeelk, D., Bendick, R., Stickney, M., & Bomberger, C. (2017). Kinematic evidence for the effect of changing plate boundary conditions on the tectonics of the northern US Rockies. *Tectonics*, *36*, 1090–1102. https://doi.org/10.1002/2016TC004427

Schwartz, D. P., Hecker, S., Stenner, H. D., Haller, K. M., Pierce, K. L., Lageson, D. R., & Machette, M. N. (2009). The 1959 Hebgen Lake, Montana, surface rupture and record of Late-Pleistocene-Holocene earthquakes. *Bulletin Geological Society of America Annual Meeting*, *41*(7), 53.

Shaw, B. E. (2011). Surface-slip gradients of large earthquakes. *Bulletin of the Seismological Society of America*, *101*, 792–804.

Stickney, M. C., & Bartholomew, M. J. (1987). Seismicity and late Quaternary faulting of the northern Basin and Range Province, Montana and Idaho. *Bulletin of the Seismological Society of America*, *77*(5), 1602–1625.

Storchak, D. A., Di Giacomo, D., Engdahl, E. R., Harris, J., Bondár, I., Lee, W. H. K., et al. (2015). The ISC-GEM global instrumental earthquake catalogue (1900–2009): Introduction. *Physics of the Earth and Planetary Interiors*, *239*, 48–63.

Thompson, S. C., Weldon, R. J., Rubin, C. M., Abdrakhmatov, K., Molnar, P., & Berber, G. W. (2002). Late Quaternary slip rates across the central Tien Shan, Kyrgyzstan, central Asia. *Journal of Geophysical Research*, *107*(B9), 2203.

Trimble, A. B., & Smith, R. B. (1975). Seismicity and contemporary tectonics of the Hebgen Lake-Yellowstone Park Region. *Journal of Geophysical Research*, *80*, 733–741.

Vallage, A., Klinger, Y., Grandin, R., Bhat, H. S., & Pierrot-Deseilligny, M. (2015). Inelastic surface deformation during the 2013 Mw 7.7 Balochistan, Pakistan, earthquake. *Geology*, *43*(12), 1079–1082.

Wallace, R. E. (1980). Degradation of the Hebgen Lake fault scarps of 1959. *Geology*, *8*, 225–229.

Wells, D. L., & Coppersmith, K. J. (1994). New empirical relationships among magnitude, rupture length, rupture width, rupture area, and surface displacement. *Bulletin of the Seismological Society of America*, *84*(4), 974–1002.

Wesnousky, S. G. (2006). Predicting the endpoints of earthquake ruptures. *Nature*, *444*, 358–360.

Witkind, I. J. (1964). Reactivated faults north of Hebgen Lake, *The Hebgen Lake, Montana, Earthquake of August 17, 1959* (Vol. 435, pp. 37–50), Geological Survey Professional Paper. Washington: U.S. Government Printing Office.

Witkind, I. J., Hadley, J. B., & Nelson, W. H. (1964). Pre-Tertiary stratigraphy and structure of the Hebgen Lake area, *The Hebgen Lake, Montana, Earthquake of August 17, 1959* (Vol. 435, pp. 199–207), Geological Survey Professional Paper. Washington: U.S. Government Printing Office.

Witkind, I. J., Myers, W. B., Hadley, J. B., Hamilton, W., & Fraser, G. D. (1962). Geologic features of the earthquake at Hebgen Lake, Montana, August 17, 1959. *Bulletin of the Seismological Society of America*, *52*(2), 163–180.

Zhou, Y., Walker, R. T., Elliott, J. R., & Parsons, B. (2016). Mapping 3D fault geometry in earthquakes using high-resolution topography: Examples from the 2010 El Mayor-Cucapah (Mexico) and 2013 Balochistan (Pakistan) earthquakes. *Geophysical Research Letters*, *43*, 3134–3142. https://doi.org/10.1002/2016GL067899

Zielke, O., Arrowsmith, J. R., Ludwig, L. G., & Akçiz, S. O. (2012). High-resolution topography-derived offsets along the 1857 Fort Tejon earthquake rupture trace, San Andreas fault. *Bulletin of the Seismological Society of America*, *102*(3), 1135–1154.

Zreda, M., & Noller, J. S. (1998). Ages of prehistoric earthquakes revealed by cosmogenic chlorine-36 in a bedrock fault scarp at Hebgen Lake. *Science*, *282*(5391), 1097–1099.